



HAL
open science

Monitoring the microstructural evolution of Nd₂Zr₂O₇ pyrochlore during dissolution at 90 °C in 4 M HCl: Implications regarding the evaluation of the chemical durability

Stephanie Szenknect, S. Finkeldei, F. Brandt, J. Ravaux, Michaël Odorico, Renaud Podor, J. Lautru, N. Dacheux, D. Bosbach

► To cite this version:

Stephanie Szenknect, S. Finkeldei, F. Brandt, J. Ravaux, Michaël Odorico, et al.. Monitoring the microstructural evolution of Nd₂Zr₂O₇ pyrochlore during dissolution at 90 °C in 4 M HCl: Implications regarding the evaluation of the chemical durability. *Journal of Nuclear Materials*, 2017, 496, pp.97-108. 10.1016/j.jnucmat.2017.09.029 . hal-02048799

HAL Id: hal-02048799

<https://hal.science/hal-02048799>

Submitted on 25 Feb 2019

HAL is a multi-disciplinary open access archive for the deposit and dissemination of scientific research documents, whether they are published or not. The documents may come from teaching and research institutions in France or abroad, or from public or private research centers.

L'archive ouverte pluridisciplinaire **HAL**, est destinée au dépôt et à la diffusion de documents scientifiques de niveau recherche, publiés ou non, émanant des établissements d'enseignement et de recherche français ou étrangers, des laboratoires publics ou privés.

Monitoring the microstructural evolution of $\text{Nd}_2\text{Zr}_2\text{O}_7$ pyrochlore during dissolution at 90°C in 4 M HCl: implications regarding the evaluation of the chemical durability.

S. Szenknect^{a*}, S. Finkeldei^b, F. Brandt^b, J. Ravaux^a, M. Odorico^a, R. Podor^a, J. Lautru^a, N.

Dacheux^a and D. Bosbach^b.

^a ICSM-UMR 5257 CNRS/CEA/UM2/ENSCM, site de Marcoule, Bât. 426, BP 17171, 30207 Bagnols/Cèze, France.

^b Forschungszentrum Jülich, Institute of Energy and Climate Research, Nuclear Waste Management and Reactor Safety (IEK-6), 52425 Juelich, Germany.

* Corresponding author. stephanie.szenknect@cea.fr

Supplementary Material available: Figure S1 and Figure S2.

Abstract

Understanding the dissolution mechanism at the solid/solution interface of $\text{Nd}_2\text{Zr}_2\text{O}_7$ pyrochlore is a critical step to evaluate its suitability to immobilize radionuclides. In this aim, the chemical durability of $\text{Nd}_2\text{Zr}_2\text{O}_7$ pyrochlore sintered samples in 4 M HCl was examined by several complementary techniques. Microstructural and structural changes were evidenced at the solid/solution interface. Environmental Scanning Electron Microscopy (ESEM), Atomic Force Microscopy (AFM) and X-Ray Reflectivity (XRR) showed that the dissolution occurs heterogeneously at the surface with a complex interplay of several dissolution rate contributors. The most important process observed is the chemo-mechanical corrosion of the pyrochlore as a consequence of the grain boundaries dissolution. The evolution of the crystal structure at the solid/solution interface was also

followed by Grazing Incidence X-Ray Diffraction (GI-XRD). It was inferred to the dissolution mechanism as a consequence of Nd and Zr occupancy of non-equivalent cationic positions in the pyrochlore structure. Regarding the chemical durability of the pyrochlore as a conditioning matrix for plutonium, minor actinides or fission products, this work demonstrates the impact of the microstructure. By increasing the grain size, and thus by decreasing the density of grains boundaries, it would be possible to limit the detachment of the grains and thus the subsequent microstructural crumbling.

1. Introduction

Several ceramics were considered as potential nuclear waste form for the specific conditioning of plutonium or fission products (1-3). The main advantage of single-phase ceramics is their capability to serve as tailor-made waste forms for the specific conditioning of radionuclides (4), (5). For many ceramic systems, natural analogues have confirmed the suitability to immobilize radionuclides for several million years (6-8). Besides monazite (9-15), apatite (16-17), thorium phosphate diphosphate (18-20), perovskite (21-22), and zirconolite (21, 23), a particular interest was dedicated to pyrochlore (24-25). Due to their high aqueous durability (26-29), chemical flexibility and radiation tolerance (8, 30), zirconate pyrochlores with the general chemical composition $A_2B_2O_7$ seem to be highly promising candidates for the immobilization of plutonium (25, 31-32).

The pyrochlore crystal structure can be derived from the fluorite structure type via the defect fluorite structure (28). Randomly removing $1/8^{\text{th}}$ of the oxygen introduces vacancies into the fluorite structure which leads to the defect fluorite crystal structure. The introduction of anionic vacancies, reduces the mean coordination number of the cations from eight to seven. The defect fluorite crystallises in the $Fm\bar{3}m$ space group. Removing oxygen atoms from well-defined lattice positions leads to the presence of two different cationic positions, A (yellow) and B (blue) (Figure 1re 1). This leads to the general pyrochlore formula $A_2B_2X_6Y$. The A cation is eightfold coordinated in a

scalenohedron shape by six X anions and two Y anions arranged. Due to the absence of $1/8^{\text{th}}$ of the oxygen the B cation is only sixfold coordinated by X anions in a trigonal antiprism. These two coordination polyhedra types are joined along edges to form the pyrochlore crystal structure. The pyrochlore crystallises in the $Fd\bar{3}m$ space group. As a result of the higher ordering of the pyrochlore structure compared to the defect fluorite structure, the lattice parameter a for the pyrochlore is twice the parameter a of the defect fluorite structure (33). The A and B positions of stoichiometric pyrochlores are each occupied by only one cationic species. Pyrochlores with more than one cation type at the A and/or B position will be referred to as non-stoichiometric pyrochlores in this work.

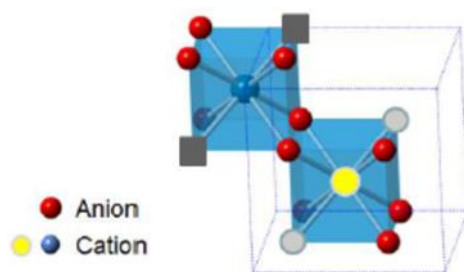


Figure 1. Anionic coordination polyhedra of a pyrochlore with the cations A (yellow), B (blue), the vacancies (grey squares), oxygen anion at the X position (red) and further oxygen ions at the Y position (light grey) (28).

The pyrochlore structure-type can accommodate a variety of A and B-site cations with valences from +II to +VI as long as reasonable ionic sizes and appropriate charge compensators are available (6, 34-36). In the framework of the nuclear waste management, pyrochlores with trivalent A sites and tetravalent B sites are of particular interest, because they can accommodate radionuclides with the oxidation states +III and +IV (25). ZrO_2 based pyrochlores were studied due to their high radiation tolerance. In contrast to the titanates, the zirconates undergo a phase transition from the pyrochlore to the defect fluorite structure as a consequence of radiation damage. A recent study discovered this mechanism to occur via a weberite structure on the local scale (37).

As a potential radwaste matrix, the chemical durability of these materials is a key property. From a thermodynamic point of view Jafar et al. (38) demonstrated the stability of uranium-substituted $Gd_2Zr_2O_7$ through high-temperature calorimetry experiments under reducing and oxidizing

conditions. From a kinetic point of view, the dissolution of synthetic ZrO_2 based pyrochlores was studied recently by Finkeldei et al. (28-29, 39). The influence of pH and temperature on the normalized dissolution rate was determined through dynamic dissolution experiments. A preferential release of Nd was observed during the early stage of dissolution. At steady state, the dissolution became congruent, and the normalized dissolution rates were found to be low and typically in the range of 4×10^{-7} to $3 \times 10^{-6} \text{ g m}^{-2} \text{ d}^{-1}$ at 90°C and $[\text{H}_3\text{O}^+] = 0.1 \text{ M}$. As noted by other authors (40-41), both chemical and physical properties of the solid surface can affect the dissolution mechanism. Measurements of macroscopic dissolution rates were thus complemented by studies of the surface after reaction by means of techniques such as atomic force microscopy (AFM) (42-48), environmental scanning electron microscopy (ESEM) (29, 49), grazing incidence X-ray Reflectivity (GI-XRR) (50-52), and light optical microscopy methods, mainly vertical scanning interferometry (VSI) (53-55). Applying these techniques provides the possibility to track the microstructural evolution of the solid/solution interface, to identify preferential dissolution zones and even to determine local dissolution rates. These approaches however, are mostly dedicated to the study of single crystals cleaved surface.

Focused on the solid/solution interface, this work thus presents a new approach to study the dissolution kinetics for $\text{Nd}_2\text{Zr}_2\text{O}_7$ ceramics in 4 M HCl solution at 90°C . The choice of the dissolution medium was based on several considerations. First, Finkeldei et al. (28, 29) determined the impact of the proton activity on the dissolution rate and demonstrated that stoichiometric pyrochlores are highly durable materials, especially at near neutral pH. As it is virtually impossible to evidence any evolution of the properties of stoichiometric pyrochlores at the timescale of laboratory experiments under conditions strictly representative of a repository site, a conservative assumption is that acidic conditions enhance the dissolution rate and thus, decrease the time necessary to observe the impact of the dissolution mechanism on the material. Second, geochemical modelling performed by Finkeldei et al. (28, 29) showed that for static experiments in 0.1 M HCl solution, the dissolution of $\text{Nd}_2\text{Zr}_2\text{O}_7$ could lead to solutions oversaturated relative to baddeleyite. It was thus decided to use 4 M HCl as a dissolution medium to observe the microstructural evolution of the pellet for shorter

dissolution time without reaching saturation of the solution relative to baddeleyite, even so the dissolution of the sample would be complete. Thus, under the conditions chosen in this study, the evolution of the microstructural properties of the $\text{Nd}_2\text{Zr}_2\text{O}_7$ ceramic was caused by the dissolution in a pure kinetic regime.

ESEM was used to evidence the evolution of the microstructure of the pyrochlore pellet at a submicron scale. Then, grazing incidence X-ray scattering was used to examine structural and microstructural modifications of the solid near the surface. By varying the incident angle, it was possible to collect reflectivity curves (below the critical angle for total reflexion) and diffraction patterns as a function of X-rays penetration depths. GI-XRR gives access to physical properties of the solid surface, as electron density and roughness of the entire sample. Whereas grazing incidence X-Ray Diffraction (GI-XRD) was used to study the structural stability of the pyrochlore material during dissolution. In addition, AFM was used to monitor changes of the solid surface topography. These complementary results were combined in order to gain a thorough understanding of the dissolution mechanism and to evaluate the chemical durability of the probed material.

2. Experimental

2.1. Preparation of $\text{Nd}_2\text{Zr}_2\text{O}_7$ pyrochlore pellets

A $\text{Nd}_2\text{Zr}_2\text{O}_7$ pellet was prepared from a powder obtained by a wet chemistry route. Details about the precipitation and a similar pellet fabrication are given in Finkeldei et al. (29). Two pellets were prepared in parallel, one for the dissolution experiment and a second for the characterization (called afterwards reference sample). After a precompaction step at 50 kN by uniaxial pressing at room temperature, both pellets were transferred into an uniaxial hot press at 1450 °C and 3.9 kN in inert atmosphere. A subsequent resintering step was applied at 1100 °C to remove the oxygen deficit. The pellet was polished with a diamond paste of 1 μm size. Via the Archimedes' method, a pellet density

of 99.5% calculated density was measured. The pyrochlore crystal structure was probed via X-ray diffraction between 10–90° 2 θ using a D4 diffractometer (θ –2 θ geometry) from Bruker AXS GmbH.

2.2. Dissolution experiments

The dissolution experiments were performed in closed PTFE containers using static conditions. They were carried out in 25 mL of 4 M HCl (prepared with 37% HCl of analytical grade from Sigma-Aldrich). These conditions were chosen on the basis of a multiparametric study of the kinetics of dissolution of Nd₂Zr₂O₇ (29, 39). These conditions prevent the precipitation of any neoformed phases at the surface of the sample, thus allow to study the dissolution far from equilibrium, in a pure kinetic regime. Moreover, the impact of the acidity of HCl solutions was demonstrated previously and a higher acidity led to an increase of the dissolution rate that allows observing microstructural and structural evolution of the solid/liquid interface at dissolution times compatible with laboratory time scale experiments. The dissolution reactor was placed in an aluminium block regulated at 90 °C. The dissolution experiments lasted about 2500 hours during which the pellet was regularly removed from the solution, washed three times with 50 mL of deionized water (18.2 M Ω .cm) to stop dissolution, and gently dried on an absorbing towel. The surface of the pellet was then characterized by GI-XRR, GI-XRD, ESEM and AFM. After the examination the pellet was again placed in the reaction container into fresh and preheated leachate.

2.3. Characterizations of the evolving interface

GI-XRR: acquisition and data treatment

GI-XRR measurements were performed using a Bruker D8 Advance diffractometer equipped with a motorized reflectivity stage that allows vertical translation of the sample. The complete primary optics setup for XRR analysis was composed of a Cu K $\alpha_{1,2}$ (λ = 1.54184 Å) source, a Göbel mirror, a motorised divergence slit, a fixed 0.2 mm slit, an automatic absorber, a fixed 0.2 mm slit after the absorber, and 2.5° Sollers slits. The data were collected with a Lynxeye detector in point mode.

Standard θ - 2θ scans were collected with a step size of 0.005° and a counting time of 7 s. The resolution of this setup was estimated to 0.01° . The background was determined for each XRR measurement using the off specular scan method (56) starting at $2\theta = 1^\circ$ with $\delta(\theta) = 0.5^\circ$ and subtracting from the collected intensity. Geometric correction in the region of the plateau of total external reflection was performed according to Salah et al. (56). Corrected intensities, I (cps) were normalized to the incident intensity, I_0 (cps). Reflectivity curves showed the evolution of the logarithm of the normalized intensity, $R = I/I_0$ versus the wave vector transfer, q (\AA^{-1}):

$$q = \frac{4\pi \sin\theta}{\lambda} \quad [1]$$

The experimental GI-XRR curves were calculated using the matrix formalism implemented in the reflex20 software (57-58). Using reflex20, only two parameters were fitted to the experimental reflectivity curves: electron density, ρ_e ($e^- \text{\AA}^{-3}$) and roughness, σ (\AA) of the substrate. Electron density of the substrate is linked to the critical wave vector transfer, q_c at which the plateau of total external reflection exhibits a strong dip:

$$\rho_e = \frac{q_c^2}{16\pi r_e} \quad [2]$$

where $r_e = 2.85 \cdot 10^{-15}$ m is the classical radius of the electron.

The fitted value of the electron density was used to determine the global porosity ε of the solid surface, since:

$$\varepsilon = 1 - \frac{\rho_e}{\rho_{e,s}} \quad [3]$$

in which $\rho_{e,s}$ ($e^- \text{\AA}^{-3}$) is the calculated electron density of the solid. Electron density and mass density ρ_s (g \AA^{-3}) are linked through:

$$\rho_{e,s} = \rho_s N_A \frac{\sum_j x_j Z_j}{\sum_j x_j M_j} \quad [4]$$

where x_j is the mole ratio of element j in the solid, Z_j (e^-) is the atomic number, M_j (g mol^{-1}) the molar mass and N_A (mol^{-1}) is the Avogadro's number.

GI-XRD: acquisition and data treatment

GI-XRD measurements were performed using the same apparatus as for the GI-XRR measurements. GI-XRD patterns were collected between 10 and 63° with a 0.02° step width for a total counting time of 15 hours in the reflection geometry. The angular domain was limited at higher angles by the beam knife-edge that equipped the reflectivity stage. The incident angle, θ_i , was fixed to a value ranging from 0.2° to 1° . By increasing the incident angle, it was possible to scan a layer of increasing thickness at the surface of the material. The penetration depth, z (\AA) of X-rays ($E = 8.048$ keV) as a function of θ_i is linked to the material absorption coefficient, β and the critical angle for total reflexion, θ_c as follows (59):

$$z(\theta_i) = \frac{-\lambda \sqrt{(\theta_i^2 - \theta_c^2) + \sqrt{(\theta_i^2 - \theta_c^2)^2 + 4\beta^2}}}{4\beta\sqrt{2\pi}} \quad [5]$$

For a compound material, the absorption term β depends on the material linear absorption coefficient, μ (cm^{-1}), which is obtained from the sum of the absorption cross sections of the constituting atoms by:

$$\beta = \frac{\lambda}{4\pi} \mu \text{ with } \mu = \rho_s \sum_j x_j \sigma_j \quad [6]$$

with σ_j ($\text{cm}^2 \text{g}^{-1}$), the total atomic absorption cross section derived from CXRO X-ray Data Booklet (60). As the density of the solid at the surface decreased during the dissolution experiments, the penetration depth of X-rays as a function of θ_i was also recalculated according to equations (2) – (4).

The quality of the PXRD patterns collected under grazing incidence was not sufficient to perform Rietveld refinement. Only qualitative observations were made in order to identify the structural evolution during the dissolution. However, some pitfalls must be avoided. According to Simeone et al. (59) the measured centroid of the Bragg peaks exhibited a shift from its theoretical value as a

function of θ_i . They demonstrated for Gd doped ceria, that this shift from the expected $2\theta_{hkl}$ angle can reach 0.15° for $\theta_i = 1^\circ$ to 0.35° for $\theta_i = 0.2^\circ$, but is relatively constant over the angular domain considered. Thus, only patterns recorded using the same incident angle were compared.

ESEM and EDX: acquisition and data treatment

The microstructural evolution of the pellet surface was monitored in operando by ESEM. The sample was disposed on the flat stainless steel sample holder without any preparation except rinsing with deionized water to avoid the presence of HCl vapour in the SEM chamber and to stop the dissolution. ESEM micrographs were recorded with a FEI Quanta 200 environmental scanning electron microscope under water pressure ranging from 250 to 400 Pa. To clean the atmosphere in the SEM, five cycles of water vapour filling between 400 and 1000 Pa were achieved. Mainly two different regions of interest were identified at the surface of the pellet and observed at several times during the dissolution experiment. ESEM micrographs of these two regions were recorded at different magnifications. Micrographs recorded at low magnification were used to evaluate the increase of the porosity. Thus, the surface area of the analysed regions reached $12\ \mu\text{m} \times 12\ \mu\text{m}$, whereas the resolution allowed the visualisation of intra and inter-granular pores. The low magnification images were processed and binarised with ImageJ 1.45m software (61). The 2D porosity was then extracted from such analysis by calculating the ratio between the surface area of the pores (black pixels) and the total surface area of the investigated domain. High magnification images were used to visualize opening of the grain boundaries and the triple junctions as the resolution of the ESEM device under environmental conditions at high magnification reached few nanometers.

Quantitative microanalyses were performed using a Bruker SDD 5010 EDX analyzer coupled with the ESEM at three different acceleration voltages (5, 15 and 30 kV). The samples were neither gold- nor carbon-coated in order to limit the absorption of the X-rays emitted during the electron-matter interaction, mainly at low voltage. As the samples are insulating, the analyses were performed under

low-vacuum conditions (50 Pa of H₂O). To perform these analyses in the best conditions, a dedicated Gaseous Analytical Detector (GAD) provided by FEI Company was used. The final aperture of this detector is located very close to the sample surface in order to improve the accuracy and spatial resolution of the X-ray analysis. Measurements of standards and samples were performed using the same configuration and counting time (120 seconds). The standard materials that were used are pure ZrO₂ and NdPO₄. The mass of oxygen was determined by stoichiometry considering Zr(IV) and Nd(III). For each acceleration voltage, five to ten analyses were performed on the pyrochlore sample after 2739 h of dissolution (end of experiment) and on the Nd₂Zr₂O₇ sample of reference. This reference sample came from the same batch of synthesis than the dissolved sample and was sintered following the same protocol. Monte-Carlo simulations of the trajectories of electrons in the sample were performed using the Casino v3.3 software (62). Images of the simulated trajectories are gathered in the Figure S1 of the supplementary material, as well as the X-rays emission profiles from Nd (MV and LIII) and Zr (LIII).

AFM: acquisition and images analysis

AFM images were recorded in tapping mode in air using a commercial Multimode8 (Bruker) apparatus. The free amplitude A_0 , varied from 1 to 1.5 Volt and the amplitude point was set around 1.2 V. Probes with nominal spring constants $k = 40 \text{ N m}^{-1}$ were used (RTESP, nominal tip radius 8 nm, resonance frequency around 300 kHz, Bruker). All images were taken at scan rates lower than 1 Hz. AFM images were flattened and analyzed using the Nanoscope 5 Analysis software (Bruker).

3. Results and Discussion

3.1. Monitoring of the microstructural evolution

A series of images of the solid surface during dissolution in 4 M HCl solution at 90 °C recorded with ESEM are depicted in Figure 2. This region of interest was selected because it was representative of the sample microstructure. The selected region appeared to be well densified. The

grain size was in the range from 0.5 to 2 μm . At intermediate magnification, the alteration of the surface appeared to be heterogeneous. Grain pull-out was observed after only 20 hours in the dissolution medium. This process occurred at different locations in the investigated surface area of the pellet for the entire duration of the experiments (for example this phenomenon is underlined by a green circle in Figure 2, 613 h). The opening of the grain boundaries (examples are indicated by blue arrows in Figure 2) and triple junctions was suspected early and became obvious after 84 hours of dissolution. The dissolution of grain boundaries occurred all over the investigated surface area of the pellet leading to additional grains pull-outs. One area of a detached grain on Figure 2 (red box, 39 h) was additionally observed at the highest magnification. The shape of the pore created by the detachment of a grain did not evolve. The comparison with the image obtained after 84 hours of dissolution showed that new sites get activated for dissolution, especially the opening of triple junctions (examples are indicated by white arrows in Figure 2) and the digging of corrosion pits within the grains was observed (indicated by yellow arrows in Figure 2). This behaviour was also noticed at various locations at the surface of the altered pellet.

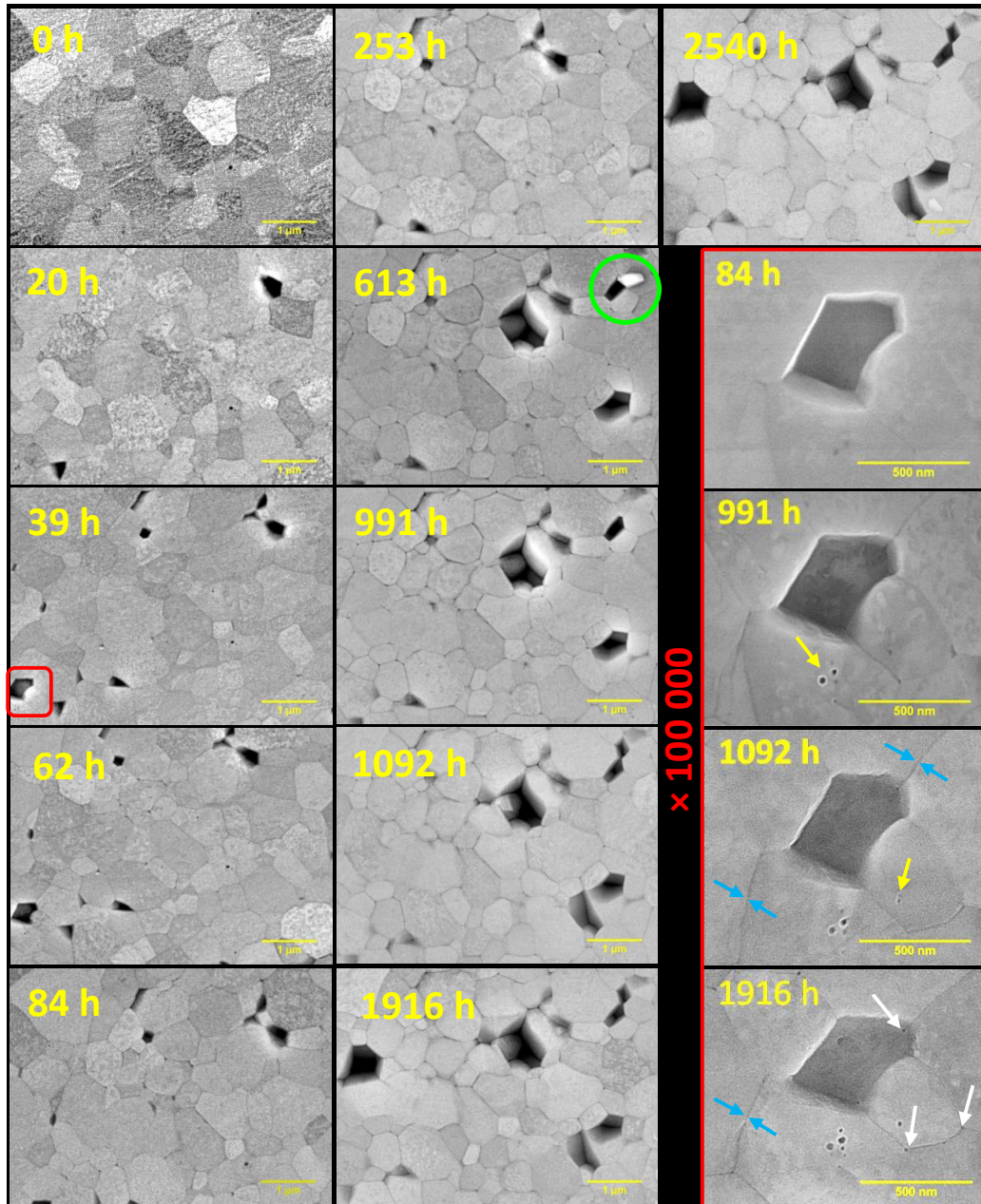


Figure 2. ESEM observations in SE mode of one selected region of interest of the $\text{Nd}_2\text{Zr}_2\text{O}_7$ sample surface during its dissolution in 4 M HCl at 90 °C. This series of images (at intermediate magnification) was used to estimate the evolution of the 2D-porosity. The green circle highlights the grain detachment. The red area indicates the position of the images monitored at the highest magnification. Blue, yellow and white arrows indicate respectively locations where the opening of the grain boundaries, the digging of the corrosion pits and the opening of the triple junctions can be seen.

ESEM images at the highest magnification presented in Figure 3, show also more clearly the modifications of single grains topography. After 613 hours of dissolution, the surface of some grains seems to change, as indicated by an orange circle, Figure 3). However, this process may have occurred earlier, as illustrated by the ESEM micrographs recorded after 62 hours presented in Figure

3. In the ESEM image recorded after 2739 hours of dissolution, it appears that some of the grains still present the same topography as prior to dissolution. Thus the surface of some grains contributed to the overall dissolution rate, whereas other grains remained the same as prior to the dissolution experiment. VSI experiments performed on the same type of ceramic pellet support the results observed by ESEM. Indeed, Fischer et al. (55) observed the formation of “flat pores” already after the short reaction period of 40 h in 4 M HCl solution at 90°C. Then, the occurrence of flat pores was increasing as well as the retreat depth that reached 60 to 115 nm after 420 hours of dissolution. VSI also showed the existence of “plateaus”, which are attributed to the existence of less reactive grains. ESEM observations were in reasonably good agreement with the results obtained by VSI, considering that “flat pores” referred to altered grains (orange circle in Figure 3), whereas “plateaus” corresponded to unaltered grains.

ESEM micrographs recorded at the highest magnification (Figure 3) also unambiguously evidenced that the material dissolution was located within grain boundaries. Obviously, the grain boundaries and triple junctions constitute preferential dissolution zones, thus confirming several observations made on other ceramic materials (49, 63-64). The weaker chemical durability of grain boundaries could be either caused by a different chemical composition than the bulk (65-67), or by a degraded crystalline order, even an amorphous state, as the junction between two crystals of different orientations led to a high concentration of defects, especially for high misorientation angle (63). For pyrochlore, the opening of the grain boundaries was first hardly detectable by ESEM, and only at the highest magnification. The ESEM images presented in Figure 3 show that the intra-granular distance generally did not exceed 2 nm, except at some locations after 2739 h of dissolution where it could reach 10 to 16 nm. The complete dissolution of the grain boundaries was clearly evidenced by the subsequent detachment of grains, the resulting pores due to the detached grains did not evolve further. This mechanism is described in the literature as chemo-mechanical corrosion of polycrystalline material.

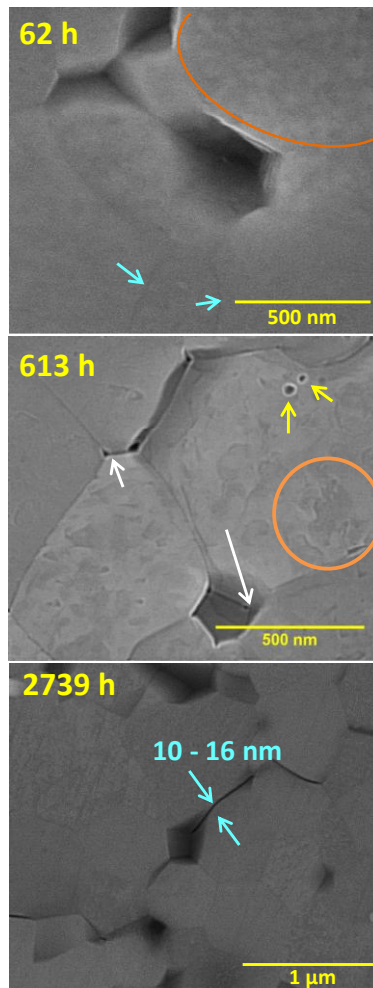


Figure 3. ESEM images in SE mode at high magnification. White arrows indicate the opening of triple junctions, yellow arrows underline corrosion pits formation or digging, orange circles highlight the grain surface alteration, blue arrows indicate the opening of the grain boundaries.

AFM images of the pellet surface were performed before and after 2739 hours of dissolution in 4 M HCl solution at 90 °C in order to better evaluate the topographic changes. Prior to dissolution, the root-mean square roughness, R_q was determined by AFM for several randomly selected areas of $4 \mu\text{m}^2$ at the surface of the same pellet and reached $1.15 \pm 0.05 \text{ nm}$, with a maximum height value of 27 nm corresponding to the presence of polishing marks (images not shown). Figure 4 shows the surface of the pellet observed after 2739 hours of dissolution under the optical microscope (Figure 4-a) and AFM (Figure 4-b and 4-c). After 2739 hours of dissolution, the solid/solution interface was strongly modified by grains pull-out. However, the initial surface was partially still present and appeared as white zones under the optical microscope (area 1 in Figure 4-a), whereas black zones corresponded to large holes created by the detachment and release of grains (area 2 in Figure 4-a).

Rq was determined with AFM for a selected region in area 1 (Figure 4-b) and reached 1.90 ± 0.02 nm, a value slightly higher than the initial one. This result indicates that the topography of the grains that are still present at the surface at the end of the dissolution experiment did not strongly evolve during the dissolution.

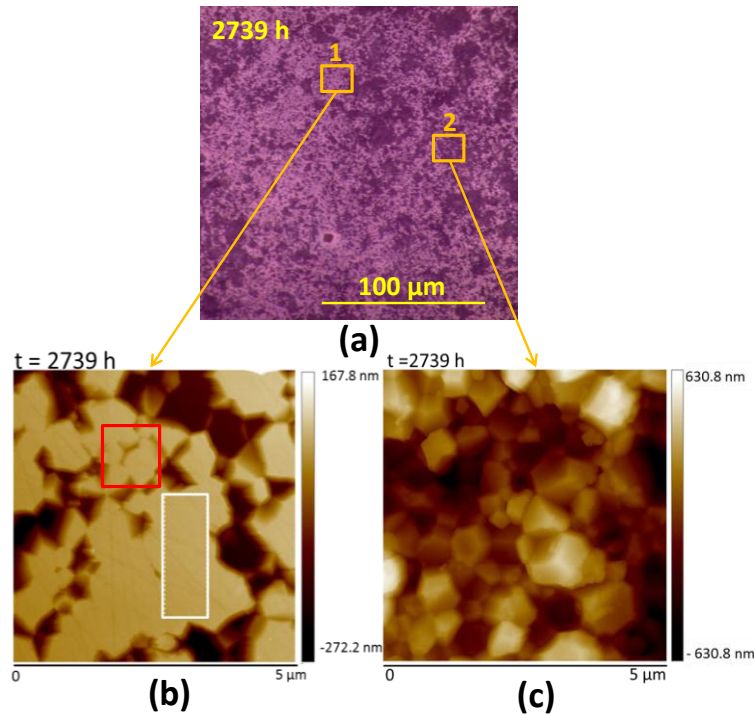


Figure 4. (a): Image of the solid surface after 2739 hours of dissolution in 4 M HCl solution at 90 °C obtained by coupling an optic microscope with the AFM, and showing the location of the two regions investigated by AFM in a larger field of view of the pellet. (b) and (c): AFM images of the surface of the pyrochlore pellet after 2739 hours of dissolution in 4 M HCl solution at 90 °C . The white square in Figure 4-b represents the selected zone for the measurement of root-mean square roughness, Rq . The red square indicates the location of the $1 \mu\text{m}^2$ image presented Figure 5.

A $1 \mu\text{m}^2$ AFM image recorded in the area 1 (red square, Figure 4-b) is presented in Figure 5-a and 5-b with the corresponding depth profiles (Figure 5-c). These profiles were compared to one depth profile recorded at the sample surface prior to dissolution. The topography of the surface of the grains (red depth profile) did not differ significantly from the initial one, indicating that these surfaces present a remarkable low reactivity. The presence of remaining polishing marks at the surface of the grains strengthened the conclusion. However, due to the absence of a reference surface, the dissolution of the surface of the grains by normal retreat was not totally excluded. The grain boundaries were hardly detectable by AFM measurements and could be easily mixed with the

polishing marks. Only one grain boundary can be identified in the blue profile Figure 5-c, which was also visible for the green profile. The formation of large holes was also evidenced (blue profiles) whose dimensions were characteristic of the grain size. The depth of these large holes can vary due to the abrasion of the grains during the polishing of the sample surface. In the area investigated by AFM, remarkable grain retreat was not detected. We assumed that the most reactive grains that could present such dissolution patterns could have been released in solution after 2739 hours of dissolution due to the intense chemo-mechanical corrosion process, thus only the less reactive grains were still present at the solid surface when AFM images were recorded.

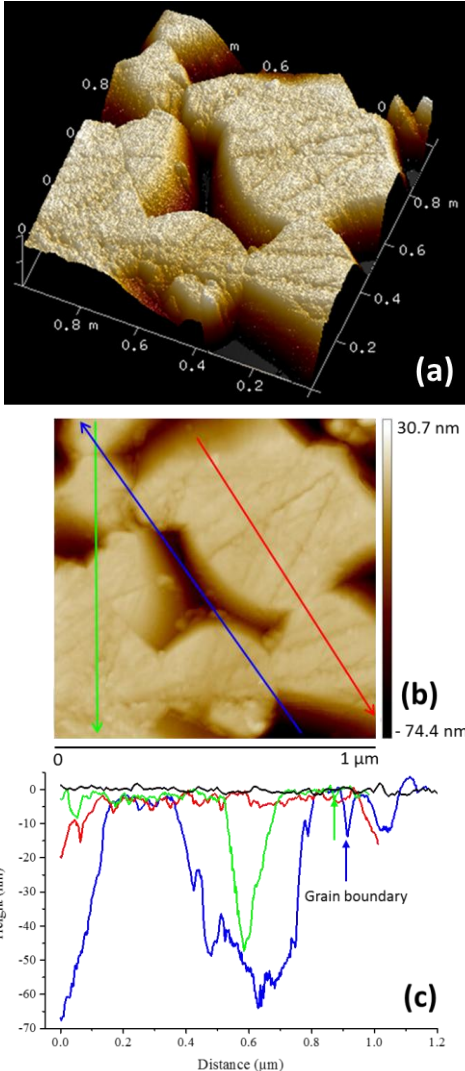


Figure 5. AFM image of $1 \mu\text{m}^2$ of surface area recorded in the white area (zone 1, Figure 4-b) after 2739 h of dissolution. (a): 3D reconstruction of the depth image, (b): corresponding depth image. (c): The depth profiles (green, blue and red) are compared with a profile representative of the initial surface (black).

The evolution of surface porosity and roughness of the surface of the pyrochlore pellet was suggested by ESEM images in Figure 2 and Figure 3. However ESEM, as all microscopic techniques, provides local information. From this point of view, XRR is a complementary technique, as the characteristic length of the microstructural details that can be detected in the direction normal to the surface is almost the wavelength of the X-ray source, whereas the surface area of the probed region is that of the sample. Thus, it gives access to a 2D-characterization of the solid/solution interface properties. The XRR curves monitored during dissolution of $\text{Nd}_2\text{Zr}_2\text{O}_7$ pyrochlore in 4 M HCl solution at 90 °C are presented in Figure 6-a. All curves show a single critical angle and a rather smooth subsequent decrease of the reflected signal. Regardless the dissolution time, neither second critical angle, nor oscillations that would be associated to the presence of a surface layer of contrasted electron density or a secondary phase precipitated at the surface of the pyrochlore pellet were observed in these curves. The alteration of the pellet surface gave rise to a decrease of the critical angle, related to the decrease of the electron density at the surface. The data were fitted with a model accounting for the evolution of the electron density and roughness of the surface of the sample. The evolution of the two parameters fitted on XRR curves during dissolution in 4 M HCl at 90 °C is presented in Figure 6-b. The roughness of the surface of the sample did not change significantly for the entire duration of the dissolution experiment. The fitted values ranged between 1.5 and 2.2 nm, which is in very good agreement with values determined with AFM before and at the end of the experiment for the less reactive assemblages of grains.

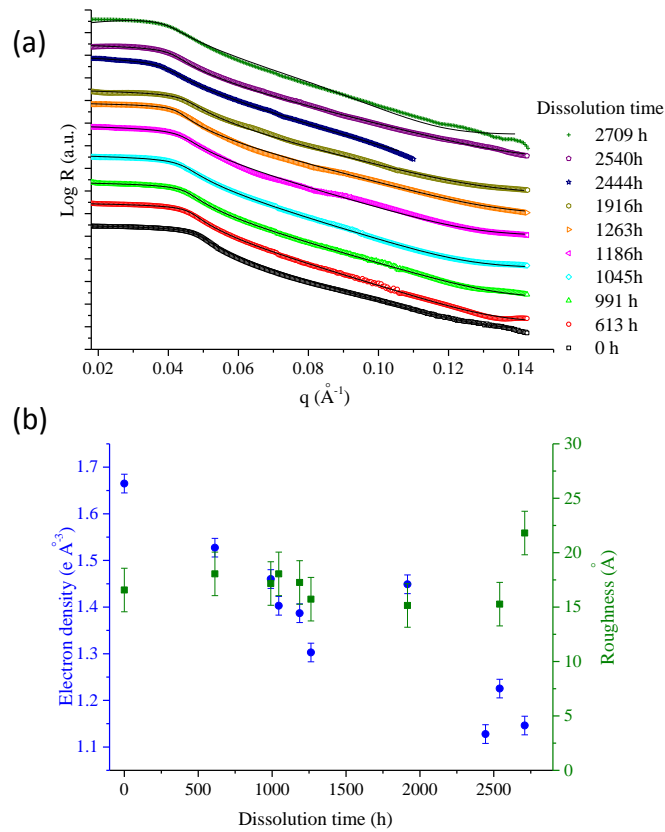


Figure 6. (a): Experimental (symbols) and simulated (lines) XRR curves obtained during the dissolution of a Nd₂Zr₂O₇ pyrochlore pellet in 4 M HCl at 90 °C. (b): Evolution of the electron density and roughness of the solid/solution interface during dissolution in 4 M HCl at 90 °C, determined by XRR.

The electron density of the surface of the sample was found to decrease strongly during the dissolution, but after 1916 hours the evolution slowed down. It is noteworthy, that the value of the electron density determined for 1916 hours of dissolution was clearly out of this trend (Figure 6-b). It is not excluded that a strong microstructural change occurred at the solid/solution interface surface at this time, probably linked with an intense release of grains in the dissolution medium. Thus, the results recorded after 1916 hours using grazing incidence X-rays would not correspond exactly to the same solid surface as before.

The porosity, ε , was obtained from equation [3], in which ρ_e is the fitted electron density of the sample (deduced from the fitted value of the critical angle) and $\rho_{e,s}$ is the value calculated from the crystallographic data. The evolution of the calculated porosity of the altered surface compared to the estimation made by ESEM micrographs analyses is shown in Figure 7.

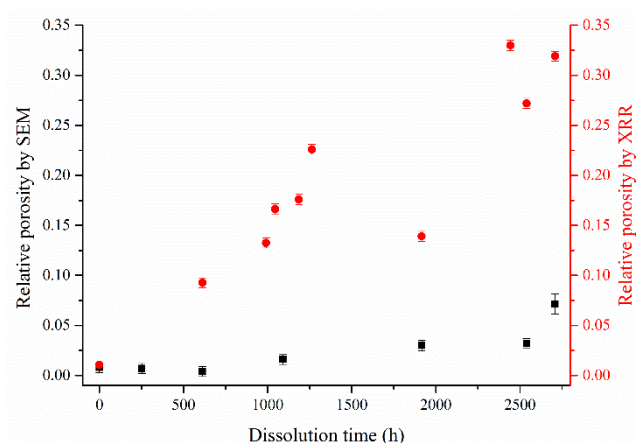


Figure 7. Evolution of the relative porosity of the solid surface during dissolution in HCl 4 M, 90 °C, determined either by XRR (red dots, secondary axis) or by ESEM images analyses (black squares).

The porosity calculated from the electron density determined by XRR increased strongly from 0.02 to 0.32. The same trend was observed by ESEM but to a lower extent. The increase of the porosity calculated from low magnification ESEM micrographs was mainly due to the grain detachments. The decrease of the electron density determined by GI-XRR could be related to the opening and digging of the grain boundaries and triple junctions and to the formation of nanometric etch pits. At low magnification, the resolution of ESEM is not sufficient to take these phenomena into account, which explains the discrepancy between both estimations of the porosity. It is also noteworthy, that the increase of the porosity determined by GI-XRR slowed down after 1916 hours of dissolution. Such behaviour could be also related to the presence at this stage of the dissolution, of mostly non-reactive grains at the solid surface that were still reflecting X-rays, whereas the most reactive grains were already released in the dissolution medium.

3.2. Monitoring the structural evolution at the solid/solution interface

GI-XRD is one of the most appropriate methods to evidence dynamic structural changes at the surface of crystallized materials (68). GI-XRD patterns with $\theta_i = 1^\circ$ were recorded regularly during the dissolution of the pellet. The recorded patterns are presented in Figure 8. The GI-XRD patterns present all the characteristic reflexes of the pyrochlore structure without any additional reflex regardless of the dissolution time. This result confirmed the absence of a crystallized neo-formed

phase as it was expected under the conditions used. In addition, the superstructural reflections characteristic of the higher ordering of a pyrochlore phase compared to a defect fluorite phase were maintained.

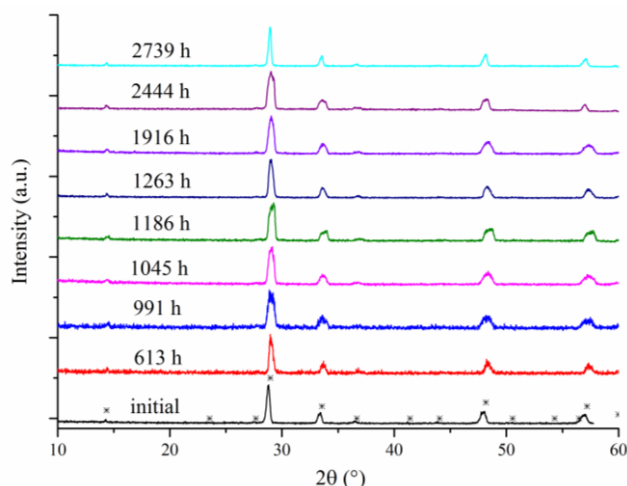


Figure 8. Grazing-incidence X-ray diffraction patterns collected at a $\text{Nd}_2\text{Zr}_2\text{O}_7$ pyrochlore sintered pellet during dissolution in 4 M HCl at 90 °C for an incident angle of 1°. * Bragg position associated to $\text{Nd}_2\text{Zr}_2\text{O}_7$ pyrochlore (JCPDS #01-078-1617).

The diffracted intensity under grazing incidence was too low to allow for Rietveld refinement of the patterns, even after long counting times (almost 15 hours per pattern). Here, only qualitative evidence can be derived from these results. To avoid misinterpretation, only the patterns recorded with the same incident angle were compared. Figure 9-a, 9-b and 9-c represent the evolution during dissolution of the position of the most intense Bragg reflection ($2\theta_{222} = 28.948^\circ$) collected at respectively $\theta_i = 0.2^\circ$, 0.4° and 1° . Interestingly, the centroid of the Bragg peak shifted towards higher theta values during the first 1186 hours of dissolution. From 1186 hours to 1916 hours the centroid of the Bragg peaks stabilized, then a decrease of the centroids position in theta values was observed and finally it approached its initial position after 2709 hours of dissolution. The shape of the Bragg peaks was also evolving during dissolution. One can note the appearance of a shoulder for the θ_{222} reflection after 1916 hours of dissolution especially for $\theta_i = 0.2^\circ$ and 0.4° (Figure 9-a and 9-b).

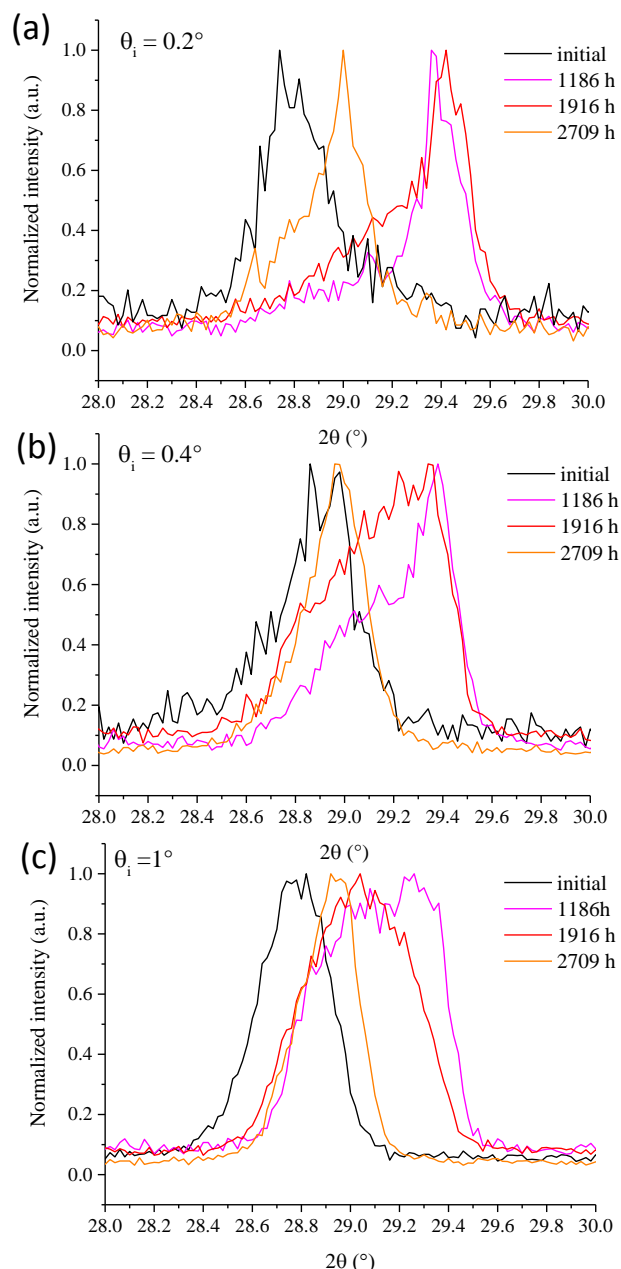


Figure 9. Evolution of the normalized most intense Bragg reflection (222) collected at a $\text{Nd}_2\text{Zr}_2\text{O}_7$ pyrochlore sintered pellet during the dissolution in 4 M HCl at 90 °C for several incident angles: (a) $\theta_i = 0.2^\circ$, (b) $\theta_i = 0.4^\circ$, and (c) $\theta_i = 1^\circ$.

The evolution of the centroid of the Bragg peaks for the θ_{222} reflection at $\theta_i = 0.2^\circ$ is illustrated in Figure 10 (similar evolution was determined for the θ_{400} and θ_{440} reflections at 0.4° and 1° and are gathered in Figure S2 of the supplementary material). The shift $\Delta(2\theta_{hkl})$ first increased, reached a maximum value in the range of $+0.7^\circ$ to $+1^\circ$ between 1100 hours and 1916 hours of dissolution, then started to decrease.

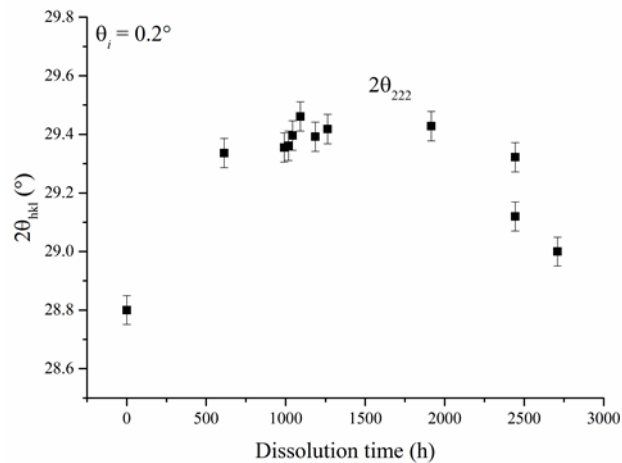


Figure 10. Evolution during the dissolution of the centroid of the Bragg peaks for the most intense Bragg reflection (222) collected at a $\text{Nd}_2\text{Zr}_2\text{O}_7$ pyrochlore sintered pellet during the dissolution in 4 M HCl at 90 °C at $\theta_i = 0.2^{\circ}$.

Qualitatively, an increase of the Bragg position could be associated with a decrease of the cell volume. In the stoichiometric pyrochlore structure ($\text{Fd}\bar{3}\text{m}$ space group), Nd^{3+} occupies the A cationic position and is coordinated by eight oxygen atoms, whereas Zr is coordinated by six oxygen atoms (33, 36). The ionic radius of Nd^{3+} in this environment reaches 1.109 Å, whereas it equals 0.72 Å for Zr^{4+} (69). A pyrochlore solid solution formation can be obtained in the range of 20.4 – 36.7 mol. % Nd_2O_3 (28). The structural changes of a stoichiometric pyrochlore to the non-stoichiometric pyrochlores as consequence of mixed Nd and Zr occupancy of the A or B site is described with the help of the antisite cation exchange model. In case of the stoichiometric composition $\text{Nd}_2\text{Zr}_2\text{O}_7$, the number of eight fold coordinated (neodymium) and six fold coordinated (zirconium) cations for the A and B position are equal. For non-stoichiometric compositions $(\text{Nd,Zr})_2\text{Zr}_2\text{O}_{7+x}$, Zr is in excess compared to Nd. Within the antisite model, Zr cations in excess are assumed to occupy the A position. The substitution of Nd by Zr is accompanied by a change of the coordination number for these Zr^{4+} cations from six to eight, which is the typical coordination number of the A position. The ionic radius of Zr^{4+} in this environment reaches 0.84 Å. Thus, in that model the effective radius of the cations in the A site decreases linearly with the neodymium depletion. This structural rearrangement could explain the first part of the evolution observed in Figure 10. The increase in the $\Delta(2\theta_{hkl})$ observed before 1100 hours of dissolution could correspond qualitatively to the decrease of the cell

volume caused by the partial substitution of Nd^{3+} by Zr^{4+} in the A site. The second part of the curve depicted in Figure 10 (i.e. the decrease in the $\Delta(2\theta_{hkl})$ shift) could be explained by the release in solutions of the most reactive grains at the surface of the pellet due to the chemo-mechanical corrosion process. Following this assumption, at the later stage of the dissolution (after 1916 hours) the proportion of non-reactive grains presenting a similar composition than before dissolution was increasing, which explains that the GI-XRD patterns get closer to the initial one. This observation (i.e. the decrease in the $\Delta(2\theta_{hkl})$ shift at late dissolution times) led to the conclusion that the remaining grains at the surface of the pellet, which were the less reactive grains from a microstructural point of view were also less affected by the structural changes evidenced by GI-XRD.

The magnitude of the shift $\Delta(2\theta_{hkl})$, was more pronounced at the lowest incident angle, corresponding to the lowest X-rays penetration depth. Figure 11 represents the evolution of the penetration depth of the X-ray beam at the most intense Bragg reflection angle ($2\theta_{222} \sim 29^\circ$) for several incident angles. For $\theta_i = 0.2^\circ$, the penetration depth increased from 50 nm to 70 nm during the dissolution experiment. In this layer, $\Delta(2\theta_{222})$ reached $+0.7^\circ$ for 1916 hours of dissolution (Figure 10). Thus, the evolution of the unit cell parameter was more pronounced at the solid/solution interface and might be linked with the dissolution mechanism.

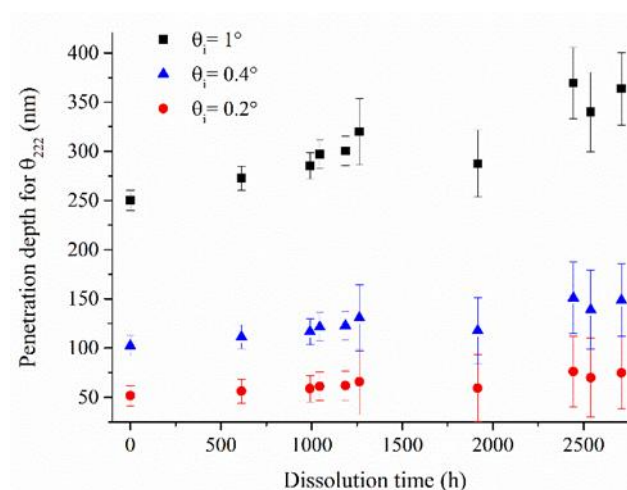


Figure 11. Evolution of the penetration depth of the X-ray beam at the most intense Bragg reflection angle ($2\theta_{222} = 29^\circ$) for several incident angles. The penetration depth was calculated using equation [5].

To test this assumption, quantitative X-EDS analyses of the pyrochlore pellet were performed at several acceleration voltages (5, 15 and 30 kV) after 2739 hours of dissolution. The results obtained after dissolution can be compared with those obtained for the non-altered $\text{Nd}_2\text{Zr}_2\text{O}_7$ reference sample. By varying the acceleration voltage, the volume of material probed by the incident electron beam changes. The lower the acceleration voltage, the lower the penetration depth. The simulated intensities of X-rays emitted by Nd and Zr as a function of depth in $\text{Nd}_2\text{Zr}_2\text{O}_7$ at the various acceleration voltages (5, 15, 30 kV) are shown in Figure S1 of the supplementary material. The average evolution of the chemical composition as a function of depth in the samples are presented in Figure 12. The Zr atomic percentage obtained at 5 kV for the dissolved sample reached 19.23 ± 0.09 at. %, whereas it was 18.79 ± 0.09 at. % for the reference sample. The Nd atomic percentage obtained at 5 kV for the dissolved sample reached 16.9 ± 0.1 at. %, whereas it was 17.5 ± 0.1 at. % for the reference sample. The results obtained at 15 and 30 kV were not significantly different for both samples. Thus, the quantitative analyse of the composition of the dissolved sample showed a small but significant enrichment in Zr of the surface of the solid even after 2739 h of dissolution, which was in agreement with the qualitative interpretation of GI-XRD patterns.

A preferential release of Nd compared to Zr was observed by Finkeldei et al. in 0.01 M to 1 M HCl at 90 °C (29, 39). The incongruent dissolution of $\text{Nd}_2\text{Zr}_2\text{O}_7$ pyrochlore was found to be more pronounced during an initial stage. Under these conditions, the normalized dissolution rate calculated from the Nd concentration in solution was one order of magnitude higher than for Zr. With time, the Nd-based dissolution rate became closer to that of Zr. This behaviour was inferred either to the possible difference in the Nd and Zr binding energy, due to non-equivalent cationic positions in the structure, or to microstructural heterogeneity. The higher coordination number of the neodymium causes a longer and therefore weaker Nd – O bond than the Zr – O bond. The degree of covalency of the Nd-O and Zr-O bonds, the cationic charge as well as the electronegativity may also be responsible for the observed preferential Nd release. The monitoring of the structural evolution of the solid/solution interface by GI-XRD and the results of the X-EDS analyses performed

at several acceleration voltages, confirmed the different behaviours of Nd and Zr regarding the dissolution mechanism and the existence of an altered surface layer with a non-stoichiometric composition.

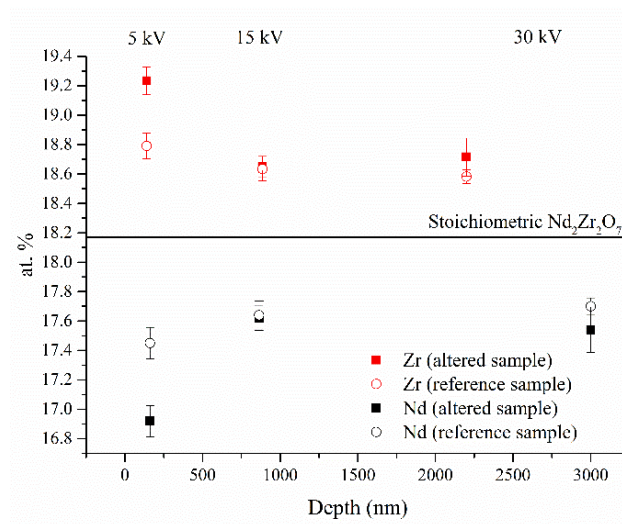


Figure 12. Variation of the chemical composition (Nd and Zr atomic %) with depth in $\text{Nd}_2\text{Zr}_2\text{O}_7$ pyrochlore after 2739 h of dissolution and in the reference sample. Depth corresponds to the thickness of material emitting 99 % of X-rays collected by X-EDS (simulations are shown in Figure S1 of the supplementary material).

3.3. Towards the dissolution scenario

The combination of the present results allows establishing a possible dissolution scenario that is illustrated in Figure 13. The evolution of the microstructure revealed a heterogeneous spatial distribution of dissolution rates. The specificity of grain boundaries and triple junctions compared to the durable bulk material was evidenced by high resolution ESEM images. This behaviour of the pyrochlore material is illustrated in Figure 13 for $t \leq 1916$ h by large red arrows. As a result of the grain boundaries dissolution, grains detachment was observed early in the dissolution, and could lead at longer dissolution times to the complete disintegration of the pellet microstructure. The release of the grains in the dissolution medium revealed fresh surfaces of grains, which can offer new sites for the progress of the dissolution process. This step in the dissolution scenario is illustrated in Figure 13 for $t \leq 2739$ h. The alteration of the surface of grains is not totally excluded, as textural modifications were observed by ESEM after 613 hours of dissolution (Figure 3 3). This process however did not concern all the grains at the solid/liquid interface, as some of the grains were found

to be mostly non-reactive, as shown by AFM images. This alteration process was not correlated to a strong increase of the roughness (R_q) of the grains, which was found to be almost constant by GI-XRR and consistent with the AFM measurements. These techniques however, provided data relative to the less reactive grains. In Figure 13, it can be seen that for long dissolution times, as a consequence of the grain detachment mechanism, the reflective surface is mostly composed of less reactive grains (in blue slashes), which can explain the constant value obtained for the roughness by GI-XRR. Another consequence of the grain detachment, the opening of grain boundaries and triple junctions is a strong increase of the porosity of the solid/solution interface as evidenced by GI-XRR and low magnification ESEM micrographs. This increase of the porosity, thus of the surface area of the solid/solution interface could also lead to an increase of the macroscopic dissolution rate during a transient step, before the dissolution of all the grain boundaries.

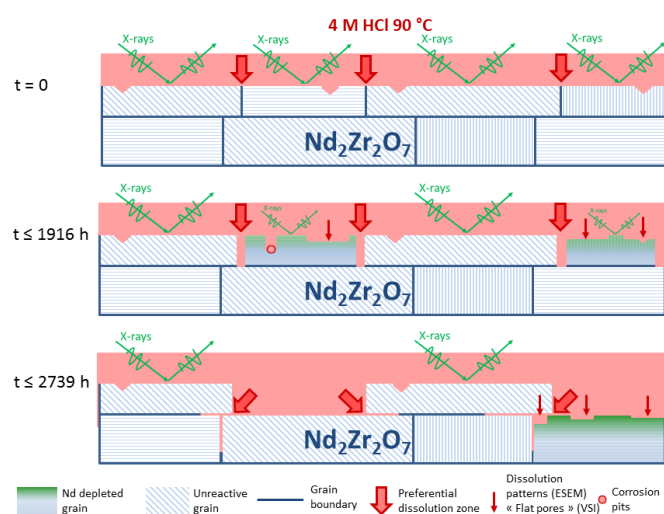


Figure 13. Schematic representation of the dissolution scenario proposed based on ESEM, GI-XRR, GI-XRD and AFM results at a $\text{Nd}_2\text{Zr}_2\text{O}_7$ pyrochlore pellet surface during dissolution in 4 M HCl solution at 90 °C (not to scale). Green arrows represent the reflection of X-rays on the surface of the grains.

An evolution of the crystal structure was also evidenced by GI-XRD, especially at low incident angles. This evolution occurred early during the dissolution and is temporally correlated to the decrease of the electron density determined by GI-XRR, the appearance of textural patterns on ESEM images recorded in BSE mode and to an incongruent dissolution step with a preferential release of Nd^{3+} in solution (29). This structural changes could affect preferentially the most reactive grains

(represented by a green to blue colour gradient, Figure 13) that are also likely to detach from the pellet. A preferential Nd dissolution would lead to a Zr enriched layer at the solid/solution interface. This non-stoichiometric pyrochlore layer presents a smaller cell volume than the stoichiometric pyrochlore as expected by the evaluation of effective cationic radius on the A site position. Finkeldei et al. (29) observed also a strong decrease of the Nd-release rate with time leading to a congruent or close to congruent dissolution. Therefore the Zr-release from the non-stoichiometric pyrochlore layer may dominate this steady state rate. Finally, such structural rearrangement of the solid/solution interface could act as a passivating layer, regarding to the Nd³⁺ release. This last stage of the dissolution scenario is however difficult to observe using surface characterization techniques as the most reactive grains are mainly released in the dissolution medium by chemo-mechanical corrosion.

4. Conclusions

By combining several techniques, it was possible to evaluate the microstructural and structural changes occurring at the solid/solution interface at a Nd₂Zr₂O₇ pyrochlore sintered pellet placed in an acidic dissolution medium. The dissolution occurs heterogeneously at the surface with a complex interplay of several dissolution rate contributors. The most important process observed is the chemo-mechanical corrosion of the pyrochlore as a consequence of the preferential grain boundaries dissolution. Parallel to the grain detachments, the dissolution of the grain boundaries, the opening of triple junctions and the digging of corrosion pits occurred, which led to an increase of the porosity of the surface and of the reactive surface area. The alteration of the surface of some grains leading to the formation of dissolution patterns evidenced by ESEM was also suspected. This process was however hardly visible for long dissolution times, due to the release in solution of the most reactive grains that present such dissolution patterns. The different behaviour of the grains could be attributed to different crystallographic orientations. A detailed study of the dissolution rates of the oriented surfaces of the grains using EBSD would allow for a more detailed analysis.

An evolution of the crystal structure at the solid/solution interface was also evidenced by GI-XRD, which could correspond to a transition from the stoichiometric to the non-stoichiometric pyrochlore structure. This evolution was inferred to the dissolution mechanism as a consequence of Nd and Zr occupancy of non-equivalent cationic positions in the pyrochlore structure. This structural rearrangement is temporally correlated to the increase of the porosity, the appearance of textural patterns for some of the grains, and to an incongruent dissolution step with a preferential release of Nd^{3+} in solution that was evidenced at the macroscopic scale (29).

The results obtained in this work show that the study of the microstructural evolution during the dissolution of ceramic material is necessary and must be coupled with the synthesis and densification steps in order to be able to elaborate a durable matrix for the conditioning of actinides. Regarding the chemical durability of the pyrochlore as a conditioning matrix for plutonium or fission products, this work demonstrates the impact of the microstructure, which is mostly controlled by the choice of the synthesis route and sintering step. By increasing the grain size, and thus by decreasing the density of grain boundaries, it should be possible to improve the chemical durability of the ceramic by limiting the detachment of the grains, the increase of the reactive surface area and the subsequent disintegration of the microstructure. However, due to the expected He built-up as a consequence of radionuclide embedding, a certain number of pores is necessary to avoid the formation of cracks within the ceramic. Therefore, a suitable compromise between the different requirements of a potential waste form matrix needs to be made. In the future, the establishment of a sintering map would be helpful to be able to control the densification rate, thus the remaining porosity, as well as the grain size of the pyrochlore pellet.

Acknowledgements

S.F. wants to thank A. Bukaemskiy for the help during the ceramic fabrication. S.S. thanks B. Corso for the technical support during the use of diffractometers.

References

1. Ringwood, A. E.; Kesson, S. E.; Ware, N. G.; Hibberson, W.; Major, A., *Nature* **1979**, 278 (5701), 219-223.
2. Weber, W. J.; Navrotsky, A.; Stefanovsky, S.; Vance, E. R.; Vernaz, E., *MRS Bulletin* **2009**, 34 (01), 46-53.
3. Donald, I. W.; Metcalfe, B. L.; Taylor, R. N. J., *J Mater Sci* **1997**, 32 (22), 5851-5887.
4. Ewing, R. C., *Progress in Nuclear Energy* **2007**, 49 (8), 635-643.
5. Anderson, E. B.; Burakov, B. E., Ceramics for the immobilization of plutonium and americium: Current progress of R&D of the VG Khlopin Radium Institute. In *Scientific Basis for Nuclear Waste Management Xxvii*, Oversby, V. M.; Werme, L. O., Eds. 2004; Vol. 807, pp 207-212.
6. Ewing, R. C., *Comptes Rendus Geoscience* **2011**, 343 (2-3), 219-229.
7. Lumpkin, G. R.; Gao, Y.; Giere, R.; Williams, C. T.; Mariano, A. N.; Geisler, T., *Mineralogical Magazine* **2014**, 78 (5), 1071-1095.
8. Lumpkin, G. R., *Elements* **2006**, 2 (6), 365-372.
9. Dacheux, N.; Clavier, N.; Podor, R., *American Mineralogist* **2013**, 98 (5-6), 833-847.
10. Terra, O.; Dacheux, N.; Clavier, N.; Podor, R.; Audubert, F., *J Am Ceram Soc* **2008**, 91 (11), 3673-3682.
11. Boatner, L. A.; Sales, B. C., *Monazite for radwaste solidification*. 1988; p 495-564.
12. Oelkers, E. H.; Poitrasson, F., *Chemical Geology* **2002**, 191 (1-3), 73-87.
13. Poitrasson, F.; Oelkers, E.; Schott, J.; Montel, J.-M., *Geochimica et Cosmochimica Acta* **2004**, 68 (10), 2207-2221.
14. Heuser, J.; Bukaemskiy, A. A.; Neumeier, S.; Neumann, A.; Bosbach, D., *Progress in Nuclear Energy* **2014**, 72, 149-155.
15. Brandt, F.; Neumeier, S.; Schuppik, T.; Arinicheva, Y.; Bukaemskiy, A.; Modolo, G.; Bosbach, D., *Progress in Nuclear Energy* **2014**, 72, 140-143.
16. Chairat, C.; Oelkers, E. H.; Schott, J.; Lartigue, J. E., *Journal of Nuclear Materials* **2006**, 354 (1-3), 14-27.
17. Chairat, C.; Schott, J.; Oelkers, E. H.; Lartigue, J.-E.; Harouiya, N., *Geochimica Et Cosmochimica Acta* **2007**, 71 (24), 5901-5912.
18. Clavier, N.; Dacheux, N.; Podor, R., *Inorganic Chemistry* **2006**, 45 (1), 220-229.
19. Clavier, N.; de Kerdaniel, E. D.; Dacheux, N.; Le Coustumer, P.; Drot, R.; Ravaux, J.; Simoni, E., *Journal of Nuclear Materials* **2006**, 349 (3), 304-316.
20. Dacheux, N.; Clavier, N.; Ritt, J., *Journal of Nuclear Materials* **2006**, 349 (3), 291-303.
21. Vance, E. R.; Lumpkin, G. R.; Carter, M. L.; Cassidy, D. J.; Ball, C. J.; Day, R. A.; Begg, B. D., *J Am Ceram Soc* **2002**, 85 (7), 1853-1859.
22. Hartmann, T.; Alaniz, A. J.; Antonio, D. J., Fabrication and properties of technetium-bearing pyrochlores and perovskites as potential waste forms. In *Atalante 2012 International Conference on Nuclear Chemistry for Sustainable Fuel Cycles*, Poinsot, C., Ed. 2012; Vol. 7, pp 622-628.
23. Deschanel, X.; Picot, V.; Glorieux, B.; Jorion, F.; Peugeot, S.; Roudil, D.; Jégou, C.; Broudic, V.; Cachia, J. N.; Advocat, T.; Den Auwer, C.; Fillet, C.; Coutures, J. P.; Hennig, C.; Scheinost, A., *Journal of Nuclear Materials* **2006**, 352 (1-3), 233-240.
24. Deditius, A. P.; Smith, F. N.; Utsunomiya, S.; Ewing, R. C., *Geochimica et Cosmochimica Acta* **2015**, 150, 226-252.
25. Ewing, R. C.; Weber, W. J.; Lian, J., *Journal of Applied Physics* **2004**, 95 (11), 5949-5971.
26. Hayakawa, I.; Kamizono, H., *Journal of Nuclear Materials* **1993**, 202 (1-2), 163-168.
27. Kamizono, H.; Hayakawa, I.; Muraoka, S., *J Am Ceram Soc* **1991**, 74 (4), 863-864.
28. Finkeldei, S. Pyrochlore as nuclear waste form: actinide uptake and chemical stability. *Schriften des Verlags im Forschungszentrums Jülich.*, 2015.
29. Finkeldei, S.; Brandt, F.; Rozov, K.; Bukaemskiy, A. A.; Neumeier, S.; Bosbach, D., *Applied Geochemistry* **2014**, 49, 31-41.
30. Lang, M.; Zhang, F.; Zhang, J.; Wang, J.; Lian, J.; Weber, W. J.; Schuster, B.; Trautmann, C.; Neumann, R.; Ewing, R. C., *Nuclear Instruments & Methods in Physics Research Section B-Beam Interactions with Materials and Atoms* **2010**, 268 (19), 2951-2959.

31. Lu, X.; Fan, L.; Shu, X.; Su, S.; Ding, Y.; Yi, F., *Ceramics International* **2015**, *41* (5, Part A), 6344-6349.
32. Icenhower, J. P.; Strachan, D. M.; McGrail, B. P.; Scheele, R. A.; Rodriguez, E. A.; Steele, J. L.; Legore, V. L., *American Mineralogist* **2006**, *91* (1), 39-53.
33. Harvey, E. J.; Whittle, K. R.; Lumpkin, G. R.; Smith, R. I.; Redfern, S. A. T., *J Solid State Chem* **2005**, *178* (3), 800-810.
34. Jafar, M.; Achary, S. N.; Salke, N. P.; Sahu, A. K.; Rao, R.; Tyagi, A. K., *Journal of Nuclear Materials* **2016**, *475*, 192-199.
35. Jafar, M.; Sengupta, P.; Achary, S. N.; Tyagi, A. K., *J Eur Ceram Soc* **2014**, *34* (16), 4373-4381.
36. Subramanian, M. A.; Aravamudan, G.; Rao, G. V. S., *Progress in Solid State Chemistry* **1983**, *15* (2), 55-143.
37. Shamblin, J.; Feygenson, M.; Neuefeind, J.; Tracy, C. L.; Zhang, F.; Finkeldei, S.; Bosbach, D.; Zhou, H.; Ewing, R. C.; Lang, M., *Nature Materials* **2016**, *15* (5), 507-+.
38. Jafar, M.; Phapale, S. B.; Mandal, B. P.; Mishra, R.; Tyagi, A. K., *Inorganic Chemistry* **2015**, *54* (19), 9447-9457.
39. Finkeldei, S.; Brandt, F.; Bukaemskiy, A.; Neumeier, S.; Modolo, G.; Bosbach, D., *Progress in Nuclear Energy* **2014**, *72*, 130-133.
40. Fischer, C.; Kurganskaya, I.; Schäfer, T.; Lüttge, A., *Applied Geochemistry* **2014**, *43*, 132-157.
41. Fischer, C.; Arvidson, R. S.; Luttge, A., *Geochimica Et Cosmochimica Acta* **2012**, *98*, 177-185.
42. Kuwahara, Y.; Makio, M., *Applied Geochemistry* **2014**, *51*, 246-254.
43. Bisschop, J.; Dysthe, D. K.; Putnis, C. V.; Jamtveit, B., *Geochimica Et Cosmochimica Acta* **2006**, *70* (7), 1728-1738.
44. Ruiz-Agudo, E.; Putnis, C. V., *Mineralogical Magazine* **2012**, *76* (1), 227-253.
45. Urosevic, M.; Rodriguez-Navarro, C.; Putnis, C. V.; Cardell, C.; Putnis, A.; Ruiz-Agudo, E., *Geochimica Et Cosmochimica Acta* **2012**, *80*, 1-13.
46. Klasa, J.; Ruiz-Agudo, E.; Wang, L. J.; Putnis, C. V.; Valsami-Jones, E.; Menneken, M.; Putnis, A., *Geochimica Et Cosmochimica Acta* **2013**, *117*, 115-128.
47. Godinho, J. R. A.; Piazzolo, S.; Balic-Zunic, T., *Geochimica Et Cosmochimica Acta* **2014**, *126*, 398-410.
48. Godinho, J. R. A.; Piazzolo, S.; Evins, L. Z., *Geochimica Et Cosmochimica Acta* **2012**, *86*, 392-403.
49. Horlait, D.; Claparede, L.; Tocino, F.; Clavier, N.; Ravaux, J.; Szenknect, S.; Podor, R.; Dacheux, N., *Journal of Materials Chemistry A* **2014**, *2* (15), 5193-5203.
50. Szenknect, S.; Mesbah, A.; Horlait, D.; Clavier, N.; Dourdain, S.; Ravaux, J.; Dacheux, N., *Journal of Physical Chemistry C* **2012**, *116* (22), 12027-12037.
51. Rebiscoul, D.; Favier, S.; Barnes, J. P.; Maes, J. W.; Martin, F., *Microelect. Eng.* **2010**, *87* (3), 278-281.
52. Rebiscoul, D.; Frugier, P.; Gin, S.; Ayrat, A., *J. Nucl. Mater.* **2005**, *342* (1-3), 26-34.
53. Green, E.; Luttge, A., *American Mineralogist* **2006**, *91* (2-3), 430-434.
54. Arvidson, R. S.; Luttge, A., *Chemical Geology* **2010**, *269* (1-2), 79-88.
55. Fischer, C.; Finkeldei, S.; Brandt, F.; Bosbach, D.; Luttge, A., *Acs Applied Materials & Interfaces* **2015**, *7* (32), 17857-17865.
56. Salah, F.; Harzallah, B.; van der Lee, A., *J. Appl. Crystallogr.* **2007**, *40*, 813-819.
57. Daillant, J.; Gibaud, A., *X-ray and Neutron Reflectivity: Principles and Applications*. Springer: Paris, 1999; p 97-115.
58. Gibaud, A.; Vignaud, G., Specular reflectivity from smooth and rough surfaces. . In *In X-ray and Neutron Reflectivity*, Springer Berlin Heidelberg: 2009; pp 85-131.
59. Simeone, D.; Baldinozzi, G.; Gosset, D.; Zalczer, G.; Berar, J. F., *Journal of Applied Crystallography* **2011**, *44*, 1205-1210.
60. Thompson, A. C., *CXRO X-ray Data Booklet* **2009**, LBNL PUB-490 Rev.3.
61. Ferreira, T.; Rasband, W., *ImageJ User Guide* **2011**, *IJ 1.45m*.

62. Demers, H.; Poirier-Demers, N.; Couture, A. R.; Joly, D.; Guilmain, M.; de Jonge, N.; Drouin, D., *Scanning* **2011**, *33* (3), 135-146.
63. Corkhill, C. L.; Myllykyla, E.; Bailey, D. J.; Thornber, S. M.; Qi, J.; Maldonado, P.; Stennett, M. C.; Hamilton, A.; Hyatt, N. C., *Acs Applied Materials & Interfaces* **2014**, *6* (15), 12279-12289.
64. Corkhill, C. L.; Bailey, D. J.; Tocino, F. Y.; Stennett, M. C.; Miller, J. A.; Provis, J. L.; Travis, K. P.; Hyatt, N. C., *Acs Applied Materials & Interfaces* **2016**, *8* (16), 10562-10571.
65. Hojo, H.; Mizoguchi, T.; Ohta, H.; Findlay, S. D.; Shibata, N.; Yamamoto, T.; Ikuhara, Y., *Nano Letters* **2010**, *10* (11), 4668-4672.
66. Matsui, K.; Yoshida, H.; Ikuhara, Y., *Acta Materialia* **2008**, *56* (6), 1315-1325.
67. Lei, Y. Y.; Ito, Y.; Browning, N. D.; Mazanec, T. J., *J Am Ceram Soc* **2002**, *85* (9), 2359-2363.
68. Hirayama, M.; Ido, H.; Kim, K.; Cho, W.; Tamura, K.; Mizuki, J.; Kanno, R., *J. Am. Chem. Soc.* **2010**, *132* (43), 15268-15276.
69. Shannon, R. D., *Acta Crystallographica Section A* **1976**, *32* (SEP1), 751-767.